ACS APPLIED NANO MATERIALS

www.acsanm.org Article

Interactions between Iron and Nickel in Fe−Ni Nanoparticles on Y Zeolite for Co-Processing of Fossil Feedstock with Lignin-Derived Isoeugenol

Zuzana Vajglová, Bibesh Gauli, Päivi Mäki-Arvela, Narendra Kumar, Kari Eränen, Johan Wärnå, Robert Lassfolk, Irina L. Simakova, Igor P. Prosvirin, Markus Peurla, Johan Kaarle Mikael Lindén, Hannu Huhtinen, Petriina Paturi, Dmitry E. Doronkin, and Dmitry Yu. Murzin*

Cite This: *ACS Appl. Nano Mater.* 2023, 6, 10064−10077 Read Online

ACCESS | Metrics & More | Article Recommendations | Supporting Information

ABSTRACT: A set of low-cost monometallic Fe, Ni, and bimetallic Fe−Ni bifunctional H−Y-5.1 catalysts with different metal ratios were synthesized by sequential incipient wetness impregnation. The catalysts were characterized in detail by N_2 physisorption, Fourier transform infrared spectroscopy with pyridine, inductively coupled plasma optical emission spectroscopy, X-ray diffraction (XRD), transmission and scanning electron microscopy (TEM−SEM), magic angle spinning nuclear magnetic resonance, X-ray photoelectron spectroscopy (XPS), Mössbauer spectroscopy, magnetic measurements, temperature-programmed reduction (TPR), and X-ray absorption spectroscopy (XAS). The results revealed that introduction of Fe led to a decrease of strong acid sites and an increase of medium Brønsted acid sites, while introduction of Ni increased the number of Lewis acid sites. The particle size of iron was approx. 5 nm, being ca. fourfold higher for nickel. XPS demonstrated higher iron content on the catalyst surface compared to nickel. Both Mössbauer spectroscopy and magnetic measurement confirmed the ferromagnetic behavior of all catalysts. In addition, the results from XRD, TEM, XPS, XAS, and magnetization suggested strong Fe−Ni nanoparticle interactions, which were supported by modeling of TPR profiles. Catalytic results of the co-processing of fossil feedstock with lignin-derived isoeugenol clearly showed that both product distribution and activity of Fe−Ni catalysts strongly depend on the metals' ratio and their interactions. Key properties affected by the Fe−Ni metal ratio, which played a positive role in co-processing, were a smaller medial metal nanoparticle size (<6 nm), a lower metal−acid site ratio, as well as presence in the catalyst of fcc FeNi alloy structure and fcc Ni doped with Fe.

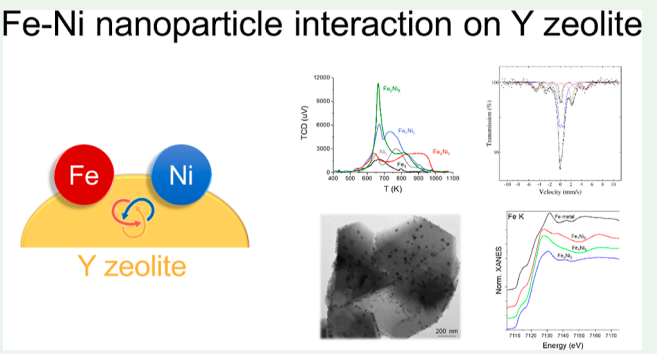

KEYWORDS: *Fe−Ni catalysts, magnetization, Mössbauer spectroscopy, TPR model, co-processing*

1. INTRODUCTION

Due to depletion of fossil-based feedstock and the environmental concerns associated with fossil fuels, lignocellulosic biomass has sparked substantial attention as a source of renewable liquid fuels and chemicals because it does not compete against food supply.[1,2] To meet the stringent sustainability and greenhouse gas emissions criteria, EU has decided to promote the use of biofuels.[3] One way to increase the use of renewable feedstock is to co-process fossil feedstock with a bioderived one and utilize the existing refinery capacity. In addition to lignocellulosic feedstock, non-edible oils, waste cooking oils, and animal fats[4] have been intensively used as a potential raw material source. Co-processing of fossil and renewable feedstocks has already been investigated to some extent[5−7] over inexpensive transition metal catalysts, such as $NiMo/Al_2O_3$[5,7] and Ni−V/zeolite.[6]

In this work, low-cost mono- and bimetallic bifunctional Fe−Ni catalysts supported on Y zeolite were synthesized and characterized, and their catalytic performance was investigated in co-processing of hexadecane with isoeugenol (Figure 1) as model compounds for fossil and renewable feedstock. Hexadecane can be both of fossil and renewable origin, while isoeugenol represents lignin-derived feedstock. Hexadecane can be produced from palmitic acid via hydrodeoxygenation (HDO) and can also originate from palm oil and several non-edible oils such as Jatropha oil.[8] Furthermore, hexadecane

Received: February 10, 2023
Accepted: May 22, 2023
Published: June 5, 2023

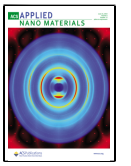

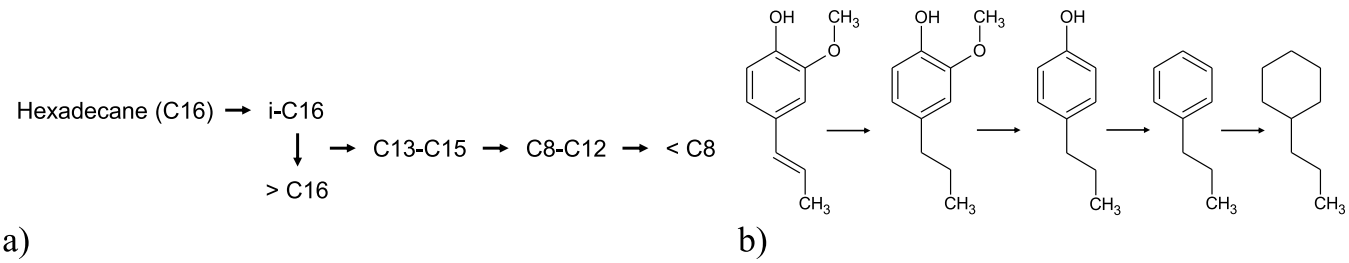

Figure 1. Scheme of (a) *n*-hexadecane hydroisomerization−hydrocracking and (b) isoeugenol HDO without a potential side reaction.

hydrocracking to jet fuel components has already been demonstrated over several H-beta-supported catalysts with Ru and Ni as active metals.[9,10]

As a catalytic support, H−Y-5.1 zeolite was selected. The high acidity of Y-5.1 zeolite makes it effective for catalyzing cracking and deoxygenation of lignin-derived compounds, while its large pore size allows diffusion of large lignin-derived molecules into the zeolite channels. Furthermore, Y-5.1 zeolite has high thermal and hydrothermal stability.

Bimetallic-supported iron and nickel catalysts have been used as active metals both in hydrocracking of oils[11] and for upgrading of lignocellulosic biomass pyrolysis vapors to value-added fuels and chemicals in a fluidized bed reactor.[12] In the fast pyrolysis process, biomass is thermally degraded in the absence of oxygen at a moderate temperature range of 723−873 K with a residence period of less than 2 s. Through this procedure, the yield of condensed bio-oil, including aldehydes, ketones, alcohols, phenolics, and other compounds, can reach up to 75%. However, this bio-oil as such is unsuitable for use as a liquid transportation fuel[13] due to low pH, instability, and high O content. A feasible technique for upgrading bio-oil from pyrolysis for fuel production could be HDO. It has been shown that monometallic Fe catalysts exhibit low activity compared to other transition or precious metals (Ni, Co, Pt, Pd, Ru, Rh, Ir, and so on.) in HDO of other lignin-derived compounds, such as guaiacol,[14−16] *m*-cresol,[17−19] or anisole,[16] that can be linked to different oxophilicity. While Co- and Ni-based catalysts demonstrated high activity in hydrogenation reactions and dihydrogen dissociation, Fe-containing counterparts displayed high activity in selective cleavage of C−O, C−OH bonds due to strong spin polarization-enhancing interactions between Fe sites and methoxy or hydroxyl groups and at the same time low activity in ring hydrogenation.[13−15,20,21] High activity and significantly enhanced selectivity to the desired products over bimetallic catalysts compared to the monometallic ones have been already shown in HDO of guaiacol over Fe−Ni supported on carbon nanotubes,[22] phenol over Fe−Ni on carbon spheres,[23] lauric acid on Fe−Ni/SiO_2,[24] anisole over Fe−Ni/zeolites,[20] and in the HDO of a simulated phenolic bio-oil consisting of phenol (50%), *o*-cresol (25%), and guaiacol (25%) over Fe−Ni/HBeta catalysts.[25]

Because bimetallic catalysts were shown to be promising for a range of potential applications,[11,20,22−24] this study is aimed at exploring potential interactions and the synergistic effects between iron and nickel nanoparticles in bifunctional Fe−Ni catalysts, with a different ratio between Fe and Ni, for co-processing of fossil feedstock with lignin-derived isoeugenol. This required performing very extensive characterization by numerous physico-chemical methods. Five different mono- and bimetallic catalysts were characterized with transmission electron microscopy (TEM), scanning electron microscopy (SEM), nitrogen physisorption, and pyridine adsorption−desorption measurements with Fourier transform infrared spectroscopy (FTIR) to study the metal particle sizes, catalyst morphology, textural properties, and acidity. In addition, to study interactions between Ni and Fe, other methods, including hydrogen temperature programmed reduction (TPR), Mössbauer spectroscopy, magnetization measurements, X-ray diffraction (XRD), X-ray photoelectron spectroscopy (XPS), and X-ray absorption spectroscopy (XAS), were applied.

Mössbauer spectroscopy was used to determine the amounts of different iron species in the bulk phase of the catalysts and to correlate the results with XPS that is sensitive to the surface composition. While Mössbauer spectroscopy has been extensively applied for monometallic Fe catalysts[26] as well as for the FeNi alloy,[27] its use for supported Ni−Fe catalysts is scarce. The existence of interactions between Ni and Fe has been confirmed by magnetization studies,[28] while applicability of XRD, which is able to reveal the presence of alloys,[29] is, however, limited by a need to have a certain metal content and not too small particle size. Furthermore, due to similar atomic scattering factors of Fe and Ni, only alloys with a crystal structure different from the structures of individual Fe and Ni can be unambiguously identified by XRD.

TPR, measures hydrogen consumption of the catalyst with increasing temperature, was applied to confirm possible interactions between the two metals in bimetallic Fe−Ni catalysts.[24,30] In terms of the metals themselves, nickel has a partially filled d-orbital and a weaker metallic bond than iron, which makes it more susceptible to lose electrons and undergo reduction. Easier reduction of nickel in comparison to iron facilitates hydrogen spillover from nickel assisting reduction of iron species. In addition to qualitative analysis of TPR data, a kinetic model for reduction of Ni- and Fe oxides based on the stoichiometry was also developed in the current study to report the corresponding rate constants and activations energies.

Catalytic properties of bifunctional catalysts were studied in a batch reactor and are reported separately.[31] In the current work, only the most pertinent catalytic data will be presented and discussed.

2. EXPERIMENTAL SECTION

2.1. Preparation of the Catalysts. To study the influence of the metal on co-processing of hexadecane with isoeugenol, a series of Fe, Ni, and Fe−Ni-supported bifunctional catalysts on a commercial H−Y-5.1 zeolitic support (nominal Si/Al = 5.1, from Zeolyst International) (Table 1) was prepared. The mono-metallic catalysts (Fe and Ni) with 5 wt % nominal metal loading were synthesized by the incipient wetness impregnation with aqueous solutions of the corresponding nitrate precursor, $Fe(NO_3)_3{\cdot}9H_2O$ (Sigma-Aldrich) or $Ni(NO_3)_2{\cdot}6H_2O$ (CJSC Souzchimprom). The bimetallic Fe−Ni catalysts containing 2−8 wt % loadings of each metal (10 wt % of the

https://doi.org/10.1021/acsanm.3c00620
ACS Appl. Nano Mater. 2023, 6, 10064−10077

Table 1. List of Catalysts, Nominal Loading

code	catalyst	metal fraction, wt %		metal fraction, mol %	
		Fe	Ni	Fe	Ni
Fe_5	5 wt % Fe/H−Y-5.1	100	0	100.0	0.0
Fe_8Ni_2	8 wt % Fe−2 wt % Ni/H−Y-5.1	80	20	80.8	19.2
Fe_5Ni_5	5 wt % Fe−5 wt % Ni/H−Y-5.1	50	50	51.2	48.8
Fe_2Ni_8	2 wt % Fe−8 wt % Ni/H−Y-5.1	20	80	20.8	79.2
Ni_5	5 wt % Ni/H−Y-5.1	0	100	0.0	100.0

total metal nominal loading) were prepared by subsequent impregnation of the H−Y-5.1 zeolite with the corresponding iron nitrate and nickel nitrate aqueous solutions and a drying step (373 K overnight) in between. Thereafter, the mono-metallic and bimetallic samples were dried at 373 K overnight and calcined at 723 K for 6 h with a temperature ramp of 2 K/min.

2.2. Characterization of the Catalysts. Micromeritics 3Flex-3500 was used to determine the textural properties. Prior to pre-treatment, the samples (ca. 0.25 g) were degassed ex situ under vacuum at 473 K for 8 h. The moisture from the catalyst was removed in this stage. The sample was then pre-treated in the physisorption equipment under vacuum at 453 K for 5 h, followed by nitrogen adsorption at −77 K and various relative pressures. The Dubinin−Radushkevich and non-local density functional theory methods were used to calculate the specific surface area and the pore size distribution, respectively.

Using pyridine (≥99%, Acros Organics) as a probe molecule, FTIR (ATI Mattson) was used for qualitative and quantitative determination of both Brønsted and Lewis acid sites. A catalyst (10−20 mg) was shaped into a thin self-supporting pellet with a radius of 0.65 cm and placed inside the FTIR cell. Pretreatment was performed at 723 K under vacuum. The temperature was decreased to 373 K after 1 h, and the background spectra were recorded. The probe molecule (pyridine) was absorbed for 30 min at 373 K before being desorbed by evacuation at various temperatures. Three desorption temperatures were designated: 523−623 K accounting for weak, medium, and strong sites, 623−723 K reflecting medium, and strong sites from which pyridine was not desorbed even at 723 K. The spectra were collected six times for each temperature ramp. The spectral bands at 1545 and 1450 cm^{-1} were used to detect the Brønsted and Lewis acid sites, respectively, during scanning under vacuum at 373 K. The molar extinction parameters reported by Emeis[32] were used to quantify the acid sites.

Inductively coupled plasma−optical emission spectrometry was used to determine the concentration of metals in the bulk of the catalyst (ICP−OES, PerkinElmer Optima 5300 DV instrument). The catalyst (ca. 0.1 g) was microwave digested in 9 mL of 30% HCl (Sigma-Aldrich), 3 mL of 65% HNO_3 (Sigma-Aldrich), and 1 mL of 50% HBF_4 (Sigma-Aldrich) mixture. After digestion, distilled water was used to dilute the sample to 100 mL.

Powder XRD was used to investigate the phase purity and for crystal phase identification of a set of Ni, Fe, and Fe−Ni catalysts supported on H−Y-5.1. The catalysts were pre-reduced ex situ with the same reduction program, as before the catalytic experiments. D8 Advance diffractometer (Bruker, Germany) with Bragg−Brentano geometry was applied. XRD patterns of samples were recorded using Cu Kα radiation (λ = 1.5418 Å) and a one-dimensional LynxEye detector with an angular range of 2.9° on the 2θ scale by scanning in the 2θ-angle range from 15 to 70° with a step of 0.05° and acquisition time of 3 s at each point. Broadening of diffraction lines was used to calculate sizes of the coherently scattering domains (CSD—D_{XRD}). The instrumental broadening of the diffraction lines was obtained by recording the diffraction pattern of the international standard α-Al_2O_3 (SRM 1976).

Jeol JEM-1400Plus with 120 kV acceleration voltage and 0.38 nm resolution and an Osis Quemesa 11 Mpix bottom-mounted digital camera were utilized to investigate the metal particle size and the textural characteristics. The catalysts were reduced using the same reduction program, as before the catalytic experiments. Determination of the metal particle sizes was performed with the ImageJ software.

SEM was used to examine the crystal morphology of the catalysts using a Zeiss Leo Gemini 1530 SEM with a Thermo Scientific UltraDry silicon drift detector (SDD).

The ^{29}Si and ^{27}Al magic angle spinning nuclear magnetic resonance spectra were recorded on a Bruker AVANCE-III spectrometer operating at 79.50 MHz (^{29}Si) and 104.26 MHz (^{27}Al) equipped with a CP−MAS 4 mm solid state probe. The ^{27}Al spectra were recorded using a 5.00 μs pulse and a recycle delay of 0.05 s at 14 kHz spinning speed. The ^{29}Si spectra were recorded using a 3.84 μs pulse and a recycle delay of 100 s at 14 kHz spinning speed.

XPS were recorded on a SPECS (Germany) photoelectron spectrometer using an Mg Kα ($h\nu$ = 1253.6 eV, 150 W) source. The binding energy (BE) scale was preliminarily calibrated by position of the peaks of gold and copper core levels: Au $4f_{7/2}$—84.0 eV and Cu $2p_{3/2}$—932.67 eV. The residual gas pressure did not exceed 8×10^{-7} Pa. The measurements were carried out after preliminary ex situ reduction of samples in the flow of molecular hydrogen (30 mL/min) according to the corresponding TPR profile 298−523 K (hold 2 h) and 523−773 K (hold 2 h) with the temperature ramp of 2 K/min followed by cooling and flushing with N_2 at room temperature, passivation with air (3 pulses during 3 min), and in situ hydrogenation [$P(H_2)$ = 10 kPa, T = 773 K, t = 1 h] in the high-pressure cell of a spectrometer at a pressure up to 101.3 kPa and temperature 323−773 K. Therewith, the samples were rubbed in a stainless steel gauze that was spot-welded on a standard holder. After cooling in hydrogen and subsequent evacuation, the samples were transferred to the analyzer chamber for measuring the photoelectron spectra. To reveal the chemical state of the elements on the surface, narrow Ni 2p, Fe 2p, as well as C 1s, Si 2p and O 1s regions were measured. The BE of the peaks were calibrated by the position of the Si 2p (BE = 103.5 eV) and C 1s (BE = 284.8 eV) peaks corresponding to the surface hydrocarbon-like deposits (C−C and C−H bonds).[33] The relative surface content of the elements and their atomic ratio were estimated from the integrated intensities of the photoelectron lines corrected for the corresponding atomic sensitivity factors (ASF).[34] The spectra deconvolution was carried out with the background estimated by the Shirley method.

The spectra of ^{57}Fe Mössbauer spectroscopy in the transmission geometry were recorded at 295 K with an 18 month-old ^{57}Co/Rh source (Ritverc Co. 50 mCi June 2020) with a maximum Doppler velocity of 11.0 mm/s. All spectra were fitted with the following Mössbauer parameters for the components: the quadrupole coupling constant eQVzz, relative intensities, isomer shift δ relative to α-Fe, and internal hyperfine magnetic field B when present, using a home-written nonlinear least-squares program. An additional Gaussian broadening for the magnetically-split components was modeled using a width ΔB of the field distribution and an experimental linewidth Γ, which was independent of the one used for the two paramagnetic Fe species. Trace Fe in the Be window of the detector were modeled using a weak quadrupole doublet with fixed hyperfine parameters slightly adjusted according to the signal-to-noise ratio of the raw gamma and X-ray spectrum of the detector.

The magnetic measurements were carried out using a Quantum Design MPMS XL SQUID magnetometer. The temperature dependence of the zero-field-cooled (ZFC) and field-cooled (FC) magnetizations was measured between 5 and 400 K with the external magnetic field of 50 mT and 1 T. The magnetic hysteresis loops were recorded at 5 and 300 K between the external magnetic fields of −2.5 and 2.5 T.

Microtrac Belcat II equipment was used to perform TPR measurements. The catalyst sample (ca. 0.25 g) was pre-treated at 473 K for 2 h in argon. It was then cooled to 323 K before being heated to 1073 K with a 5 K/min ramp under 1.5 mL/min of hydrogen and 28.5 mL/min of argon (5 vol % H_2 and 95 vol % Ar).

https://doi.org/10.1021/acsanm.3c00620
ACS Appl. Nano Mater. 2023, 6, 10064−10077

Table 2. Brønsted and Lewis Acid Sites of Fe, Ni, and Fe−Ni/H−Y-5.1 Catalysts[a]

catalyst	BAS				LAS				TAS	B/L
	w	m	s	∑	w	m	s	∑	μmol/g	
H−Y-5.1[36]	47	85	21	154	8	3	7	18	172	9
Fe_5	106	194	0	301	6	6	0	12	313	24
Fe_8Ni_2	53	60	0	113	46	1	0	47	160	2
Fe_5Ni_5	42	113	0	155	74	33	0	107	262	1
Fe_2Ni_8	8	101	0	109	51	21	0	73	182	2
Ni_5	51	89	21	161	129	22	13	165	326	1

[a]BAS—Brønsted acid sites, LAS—Lewis acid sites, TAS—total acid sites, B/L—ratio of the Brønsted and Lewis acid sites, s (strong acid sites, data at 723 K), m (medium acid sites, data at 623 K minus data at 723 K), and w (weak acid sites, data at 523 K minus data at 623 K). Data reproducibility of catalyst acidity was measured with a relative error of less than ±5%.

Table 3. Metal Concentration Determined by ICP−OES and Median Metal Particle Sizes (Fe, Ni) Determined by TEM (d_{TEM}) and Average Metal Particle Size (Fe, Ni) Determined by XRD (d_{XRD})

catalyst	metal concentration		metal fraction				$d_{XRD,\ fresh}$	$d_{TEM,\ fresh}$
	wt %		wt %		mol %		nm	nm
	Fe	Ni	Fe	Ni	Fe	Ni	Fe, Ni	Fe, Ni
Fe_5	4.5		100.0		100.0		<3[a]	5.4
Fe_8Ni_2	7.2	1.8	79.7	20.3	80.5	19.5		6.3
Fe_5Ni_5	4.4	4.4	49.8	50.2	51.1	48.9	<3[a](Fe), 9 (Ni)	11.0
Fe_2Ni_8	1.8	7.4	19.3	80.7	20.1	79.9		4.6
Ni_5		4.5		100.0		100.0	17	19.2

[a]XRD reflex of Fe-containing crystal phase not visible in XRD pattern, apparently the CSD size is below 3 nm. The relative error of ICP−OES was less than ±0.3%.

XAS, in terms of X-ray absorption near edge structure (XANES) and extended X-ray absorption fine structure (EXAFS), was used to study bulk-averaged element-specific local structure around Fe and Ni atoms. Measurements were performed on calcined and reduced (quasi in situ) bimetallic catalysts. For reduction, the catalyst samples were placed in a quartz capillary, 1.5 mm o.d., 0.02 mm wall thickness, and sample bed length 3 mm. Neat H_2 was flowing through samples at 20 mL/min flow rate. The samples were heated by means of a hot air blower from 273 to 523 K with a dwell time of 2 h and subsequently from 523 to 773 K (2 h dwell time) with the temperature ramp of 2 K/min. After that the sample holders were sealed by means of two-way valves (Swagelok), packed in polyethylene bags using a vacuum food sealer, and transported for the measurements to be taken place approximately 48 h later. XAS spectra at Fe and Ni K absorption edges were recorded at the P65 beamline of PETRA III synchrotron radiation source (DESY, Hamburg) in transmission mode. Higher harmonics were rejected by a pair of Si plane mirrors installed in front of the monochromator. The energy of the X-ray photons was selected by a Si (111) double-crystal monochromator and the beam size was set by means of slits to 0.3 (vertical) × 1.5 (horizontal) mm^2. XANES were normalized and the EXAFS spectra background subtracted using the Athena program from the IFEFFIT software package.[35] The k^2-weighted EXAFS functions were Fourier transformed (FT) in the k range of 2−14 $Å^{-1}$ and multiplied by a Hanning window with a sill size of 1 $Å^{-1}$. The displayed FT EXAFS spectra were not corrected for the phase shift. For the structure refinement amplitude, reduction factors S_0^2 0.65 (Fe) and 0.81 (Ni) were obtained by fitting the Fe and Ni foil reference spectra. The fits of the EXAFS data were performed using Artemis[35] by a least square method in R-space between 1.0 and 3.0 Å. Coordination numbers (CN), interatomic distances (r), energy shift (δE_0), and mean square deviation of interatomic distances (σ^2) were refined during fitting. The absolute misfit between theory and experiment was expressed by ρ.

3. RESULTS AND DISCUSSION

3.1. Textural Properties. The textural properties of Fe, Ni, and Fe−Ni/H−Y-5.1 catalysts are given in Table S1. The specific surface area of the pristine H−Y-5.1 zeolite was ca. 900 m^2/g.[36] After the metal introduction, the specific surface area and pore volume decreased by more than 40% due to blocking of relatively large-sized pores and channels of H−Y-5.1[25] by Fe and Ni metal nanoparticles. All catalysts exhibited a type IV isotherm (Figure S1a) with almost all of the pore volume being in the micropore range (Figure S1b).

3.2. Acidity. Acidity of the catalysts was determined by FTIR with pyridine (Table 2).

Comparison with the pristine support clearly showed that introduction of Fe led to a decrease of strong acid sites simultaneously increasing, mainly, medium Brønsted acid sites. An increase of the weak and medium Brønsted acid sites could be explained by different oxidation states of iron. Iron, particularly in its high oxidation state (Fe^{3+}), has a relatively high affinity for protons and can act as a proton acceptor, which can lead to an increase in the number of Brønsted acid sites in a catalyst. While existence of Lewis acidity for α-Fe_2O_3 is known,[37] in the current case, complete disappearance of the strongest acid sites (Brønsted and Lewis) with higher affinity for metal species[38] was observed. This behavior can be due to interactions of iron species with the acidic sites on the zeolite surface, such as coordination with oxygen atoms or hydroxyl groups, modification of the electronic structure of the zeolite surface, and formation of metal clusters that occupy or block the active sites. Complete disappearance of the strongest acid sites was also previously observed in ref 38 where the authors described the changes in the distribution of the acid site strengths to the interactions between Pt crystallites and the zeolitic support. Introduction of Ni resulted in increasing weak and medium Lewis acid sites. Therefore, monometallic Fe catalyst exhibited the highest amount of Brønsted acid sites, 301 μmol/g, with the highest ratio of the Brønsted to Lewis acid sites (B/L = 24). Conversely, the highest amount of Lewis acid sites, 165 μmol/g, and the B/L ratio equal to unity were observed for the monometallic Ni catalyst.

https://doi.org/10.1021/acsanm.3c00620
ACS Appl. Nano Mater. 2023, 6, 10064−10077

Table 4. Surface Atomic Composition of Elements and the Percentage Composition of Metals Species by Valence State on the Surface of Fe, Ni, and Fe−Ni/H−Y-5.1 Catalysts Determined by XPS and the Valence State of Fe in the Bulk of Catalysts Determined by Mössbauer Spectroscopy

catalyst	atomic ratio of elements				on the surface				in the bulk		
	Ni/Fe	Fe/Si	Ni/Si	O/Si	Ni^0	Ni^{2+}	Fe^0	Fe^{2+}	Fe^0	Fe^{2+}	[a]Fe^{3+}
Fe_5		0.02		1.99			0	100	29	25	46
Fe_8Ni_2									35	0	65
Fe_5Ni_5	0.77	0.02	0.016	1.85	46	54	17	83	22	26	52
Fe_2Ni_8									43	9	48
Ni_5			0.042	1.96	43	57					

[a]Mainly Fe^{3+}.

3.3. Metal Concentrations. The real metal concentrations, determined by ICP−OES, were slightly lower than the nominal values (Table 3). However, the metal ratio remained the same.

3.4. X-ray Diffraction. The XRD patterns of the monometallic Fe, Ni, and bimetallic 5−5 wt % Fe−Ni/H−Y-5.1 catalysts clearly indicated the FAU zeolite type with the particle size >100 nm (Figure S2). At 2θ = 44.7° and 2θ = 51.9°, the nickel phase was identified, which can be attributed to Ni^0 (1 1 1) and (2 0 0), respectively.[19,39] On the contrary, no iron phase was detected, which could be attributed to the uniform dispersion of Fe as well as the inefficient Fe oxide reduction at 773 K.[30] Similar results were also obtained for Fe_2O_3/Y,[40] Fe/ZSM-5,[41] FeNi/H−Y, FeNi/MCM-41, FeNi/γ-Al_2O_3, and FeNi/H-beta catalysts[42] with Fe loading lower than 9 wt %. In comparison to the monometallic Ni-catalyst, the intensity of diffraction lines in the Fe_5Ni_5 bimetallic catalyst decreased due to the addition of NiO. This could be related to the presence of Fe oxides causing a better dispersion of NiO, indicating interactions between Fe and Ni oxides.[30]

3.5. Electron Microscopy. The median metal particle sizes (Fe, Ni) were determined by TEM (Table 3). The TEM images and the metal particle size distribution of the fresh catalysts are displayed in Figure S3. For the monometallic Fe-catalyst, the smallest metal particle sizes (5.4 nm) were detected, as well as a narrow particle size distribution (1−25 nm). Analogous results were reported for 8 wt % Fe/H−Y zeolite (5 nm Fe_2O_3).[40] On the contrary, for the monometallic Ni-catalyst, the largest metal particle sizes were observed. The presence of Fe in the bimetallic catalyst shifted the particle size distribution to smaller particles compared to the monometallic Ni/H−Y-5.1. This could be related to the stabilizing and geometric influences of iron−nickel interactions.[23] It is in line with XRD results and the data reported in ref 43 stating that dispersion and stability of the active metallic sites were improved by the presence of the second metal as a promoter to diminish metal sintering. However, it should be noted that in these TEM images, nanoparticles of Fe and Ni could not be separated from each other in the bimetallic catalysts.

According to the XAS measurement, described below, a significantly smaller median particle size of FeNi determined by TEM for Fe_2Ni_8 compared to Fe_5Ni_5 could be attributed to the presence of relatively small particle sizes of fcc Ni doped/alloyed with Fe (ca. 1.2 nm) and bcc Fe doped with Ni (1.3−1.5 nm) in Fe_2Ni_8 compared to the fcc FeNi random alloy structure present in both catalysts.

SEM images of pristine H−Y-5.1 zeolite and the fresh Fe, Ni, and Fe−Ni/H−Y-5.1 catalysts (Figure S4) confirmed presence of well-defined zeolite crystallites, which retain their shapes and the average crystal sizes after the metal introduction as well as after the reaction (4 h). The average particle sizes determined by SEM were 500−600 nm, which is in line with XRD results (>100 nm).

3.6. Nuclear Magnetic Resonance Spectroscopy. The Si spectrum for the pristine zeolite (black in Figure S5) has three distinct peaks with the shifts at ca. −97 (16%), −103 (43%), and −108 (41%) ppm corresponding to Si present as $2Si_2Al$, $3Si_1Al$, and 4Si, respectively.[44] These peaks are clearly changed with the addition of metals, resulting in an increase of intensity for the peak at −108 ppm. For Ni/H−Y-5.1, the peak at −108 ppm increases slightly to 43% at the expense of the peak at −97 ppm, and for Fe/H−Y-5.1, the contribution of 4Si peak at −108 ppm elevates even more to 59%, lowering other peaks, i.e., 7 and 34% for the peaks at −97 ppm and at −103 ppm, respectively. The most significant change has been observed when both metals have been added to the catalyst, resulting in the dominance (85%) of the signal at −108 ppm corresponding to 4Si while contribution of other peaks is 3% (−97 ppm) and 12% (−103 ppm). Interestingly, this large change in the Si peaks was observed when both Ni and Fe have been introduced to the catalyst, while for monometallic zeolites, the peak at −108 ppm increased by merely 2−18%.

Because of the limitations imposed by the magnet applied in the measurements as well as overlapping of the peaks, interpretations of the changes in the ^{27}Al spectra are not straightforward. In general, it is agreed that the peak corresponding to the extra-framework octahedral alumina is located at 0 ppm.[45] This peak was disappearing with the addition of metals, except for the Fe monometallic catalyst, where a small peak at 0 ppm is still present. The peaks at 60−52 ppm correspond to tetrahedral alumina.[46] The intensity of the peak at a lower ppm (ca. 52 ppm) upon addition of only one metal (Ni or Fe) was much lower than in the case of the bimetallic catalyst. Overall, the NMR spectra point out on the changes in structure of the parent zeolite upon introduction of the metals.

3.7. Photoelectron Spectroscopy. The prepared reduced catalysts Fe_5, Fe_5Ni_5, and Ni_5 were investigated by XPS. Figure S6a compares full survey XPS scans (0−1200 eV) for all catalysts indicating the presence on the surface Ni, Fe, Si, and O species. The intensities of Al species are rather low despite the SiO_2/Al_2O_3 molar ratio of 5.1 for H−Y-5.1 (Figure S6a). To discuss the valence state of the metals (Fe and Ni) in three types of catalysts, the individual regions for iron (700 eV/723 eV) and nickel (844 eV/872 eV) are shown in Figure S6b,c. The Fe (711.0 and 707.3 eV for Fe $2p_{3/2}$) and Ni (855.9 and 853 eV for Ni $2p_{3/2}$) species were detected, with the surface atomic composition from XPS displayed in Table 4.

XP spectrum of the reduced monometallic Fe_5 catalyst is characterized by the Fe $2p_{3/2}$ peak near 711.0 eV with a

https://doi.org/10.1021/acsanm.3c00620
ACS Appl. Nano Mater. 2023, 6, 10064−10077

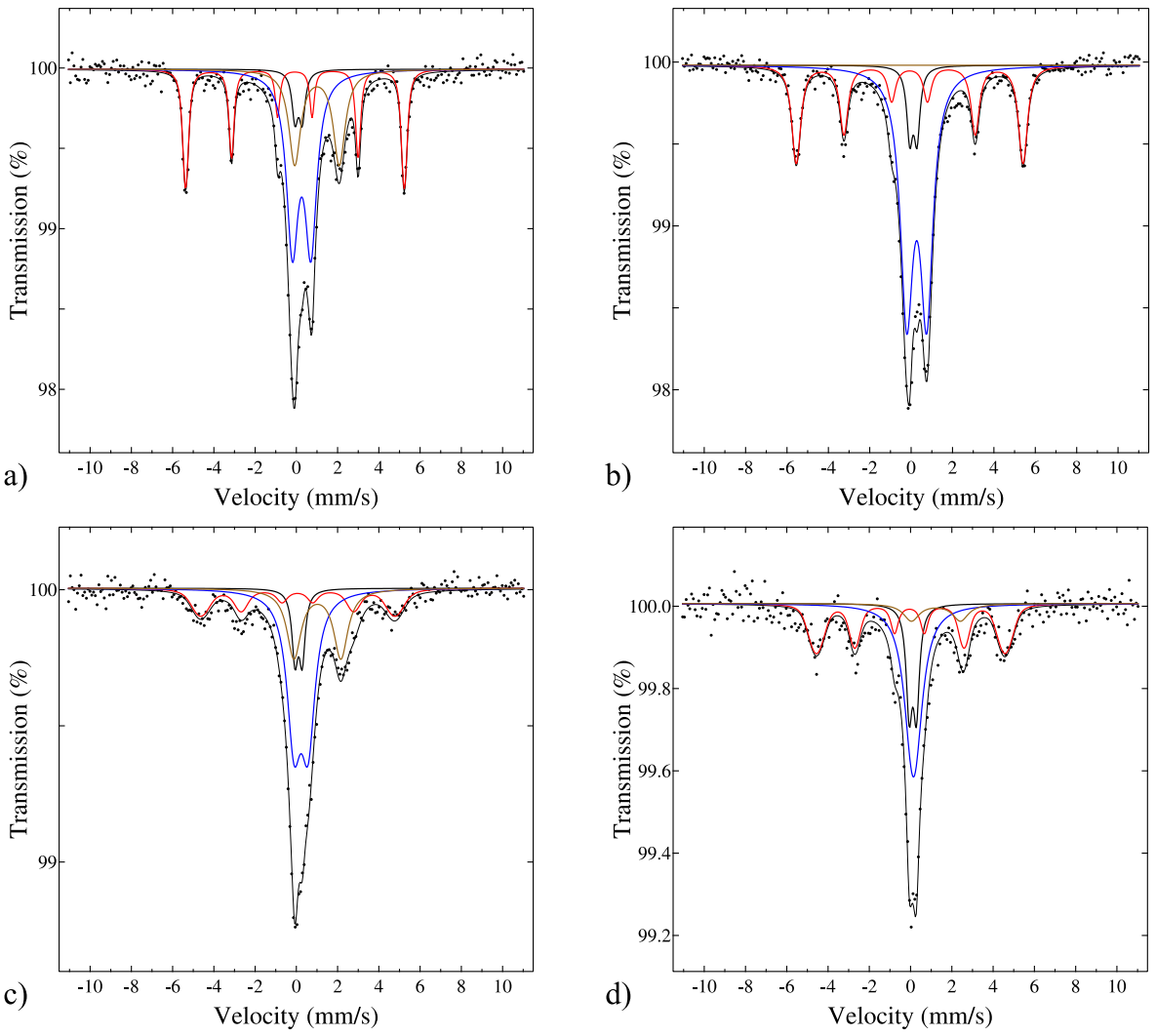

Figure 2. Mössbauer spectra of Fe and Fe−Ni/H−Y-5.1 catalysts: (a) Fe_5, (b) Fe_8Ni_2, (c) Fe_5Ni_5, and (d) Fe_2Ni_8. Legend: metallic and magnetic Fe (red), Fe^{2+} (beige), Fe^{3+} (blue), and Fe impurity in detector (black).

corresponding satellite at a higher (BE ∼ 715.5 ± 0.2 eV) indicating that Fe exists mainly in the form of oxidized Fe^{2+} species on the catalyst surface.

After reduction of the bimetallic Fe_5Ni_5 catalyst, an additional peak corresponding to metallic Fe species near 707.3 eV appeared (Figure S6b) accounting for up to 17% (Table 4). It can be clearly seen that introduction of Ni to Fe catalyst resulted in the formation of the metallic iron implying that Ni addition either facilitated reduction of iron oxide or alternatively improved resistance of the latter to oxidation after exposure to air.

XP spectra of the reduced monometallic Ni-catalyst in Ni $2p_{3/2}$ region displayed the Ni peak near 855.9 eV due to Ni^{2+}; whereas, the peak near 853.0 eV implies presence of metallic Ni^0 (Figure S6c) accounting for 57 and 43%, respectively (Table 4). In the pre-reduced Fe_5Ni_5, Ni^{2+} and Ni^0 species are both detected with the corresponding peak areas of 54 and 46%, similar to that in the monometallic catalyst, even though the area of the Ni peaks in Ni $2p_{3/2}$ region was twice as lower in comparison with Ni_5 catalyst. Note that, contrary to XPS surface composition, bulk Ni loading was approximately the same in mono- and bimetallic catalysts, 4.53 and 4.40 wt %, respectively, according to ICP−OES (Table 3). The presence of Fe did not affect the binding energies of Ni^0 and Ni^{2+} peaks in Ni_5 and Fe_5Ni_5 catalysts (Figure S6c).

Taking into account the presence of both Fe and Ni in metallic states, formation of Fe−Ni alloy in the Fe_5Ni_5 catalyst cannot be excluded.[47,48] The surface atomic ratios Ni/Fe, Fe/Si, Ni/Si, and O/Si from the quantitative XPS analysis are displayed in Table 4. According to these calculations, the Fe/Si species atomic ratio for mono- and bimetallic catalysts did not change while the atomic ratio Ni/Si decreased in the latter more than twofold (Table 4). Note that according to ICP−OES, the bulk Fe and Ni metal contents were ca. 4.4 wt % in Fe_5Ni_5 catalyst (Table 3) corresponding to Ni/Fe atomic ratio 0.96, which is slightly different from their surface atomic ratio 0.77 detected by XPS (Table 4), indicating that more iron was present on the surface.

3.8. Mössbauer Spectroscopy and Magnetic Measurements. In the Mössbauer spectrum of fresh reduced Fe and Fe−Ni/H−Y-5.1 catalysts, one resolved sextet of metallic and magnetic Fe clusters, one doublet of Fe^{2+}, and one singlet or doublet compatible with Fe^{3+} can be easily identified (Figure 2). These observed two doublets are typical of paramagnetic high spin Fe (2+ and 3+). The percentage composition of iron species, assuming equal recoil-free

https://doi.org/10.1021/acsanm.3c00620
ACS Appl. Nano Mater. 2023, 6, 10064−10077

absorption, by their valence state is reported in Table 4. These results would indicate the presence of more than 46% of Fe^{3+} in all samples, although this phase was not detected at all on the surface of the catalysts by XPS. This could be related to the reduction temperature of 773 K at which initial Fe^{3+} (originated from $Fe(NO_3)_3{\cdot}9H_2O$ precursor) was fully reduced on the surface but only partially reduced in the bulk of the catalyst. The monometallic Fe-catalyst exhibited substantial presence of all three iron phases. Comparison of its Mössbauer spectrum with the bimetallic Fe−Ni catalysts clearly showed, e.g., judging by the distance between lines 1 and 6 in the sextets, that diluting iron with nickel broadens the lines and decreases the internal magnetic field strength (B) (Table S2). However, a decrease of B was not directly related to the Ni content in the sample. Therefore, it should be mentioned that an increased metal particle size led to a decrease in the internal magnetic field strength. The Fe_2Ni_8 catalyst had very little divalent Fe, and Fe_8Ni_2 had practically no divalent Fe, while Fe_5Ni_5 was not so rich in metallic Fe. The presence of metallic Fe confirms the ferromagnetic behavior of the samples.

The Mössbauer parameters influenced by the chemical state of iron, such as the isomer shift, δ, quadrupole splitting, ΔEQ, internal hyperfine magnetic field, B, and iron magnetic moment, μ_{Fe}, are shown in Table S2. A slightly higher value of the isomer shift was observed for the metallic and magnetic Fe clusters in the Fe_5Ni_5 catalyst, as compared to the others, which could be partially due to strong broadening, affecting the accuracy. On the contrary, the isomer shift of Fe^{3+} decreased (from 0.39 to 0.26 mm/s) with increasing amount of Ni in the sample. The value related to the monometallic Fe/H−Y-5.1 catalyst is in the range of values obtained for the monometallic Fe catalyst supported on H-beta, H-ZSM-5, and H-MOR zeolites ($\delta_{Fe^{3+}}$ 0.24−0.37 mm/s).[26] However, for these monometallic Fe-catalysts, the magnetic hyperfine field was only ca. 13 T, which was explained by an amorphous character of iron oxide nanoparticles.[26] In the current work, the monometallic Fe-catalyst reached 33 ± 0.1 T of magnetic field, which is the value for α-Fe (33.0 T). In the case of the bimetallic Fe−Ni catalysts, the magnetic field decreased from 34.0 to 28.4 T with increasing amount of Ni in the sample. Differing values can be due to, e.g., Ni replacing one nearest-neighbor Fe atom. The varying number of the Ni nearest neighbors then led to a distribution of hyperfine field values observed, resulting in broadening of the absorption lines. Similar values (29.8−33.0 T) were also obtained for FeNi alloy films with the 1:1 atomic ratio of metals.[27] A slightly higher B of 34.8−35.5 T was obtained for Fe−Ni−Ti alloys.[49]

In order to test the aforementioned hypothesis resulting from Table 4 that Fe^{3+}, being reduced on the surface, is only partially reduced in the main part of the catalyst, additional measurements were performed at 77 and at 77 K in a field of 600 mT for Fe_5Ni_5 (Figure S7). The trend was clear, namely, that the component assigned to Fe^{3+} had lost its intensity and, instead, the magnetic sextet assigned to metallic Fe had increased. At 300 K, the fraction of $*Fe^{3+}$ was 52% decreasing to 24% at 77 K and finally reaching only 19% when the field was switched on. However, the paramagnetic $*Fe^{3+}$ component (in blue in Figure S7) did not vanish entirely, indicating that some trivalent Fe could exist in the bulk. The behavior, where metallic Fe gives a paramagnet signal at room temperature, indicates the presence of superparamagnetism or some kind of a spin-glass or cluster-glass phase rather than oxidation.

The curves from mass magnetization as a function of magnetic induction determined at 5 and 300 K are depicted in Figure S8. Saturation magnetization (Ms, maximum induced magnetization), remanent magnetization (Mr, induced magnetization remaining after an applied field is removed), and coercivity (Hc, the intensity of an external coercive field needed to force the magnetization to zero) of Fe, Ni, and Fe−Ni/H−Y-5.1 catalysts at two different temperatures are reported in Table S3. The magnetic induction-dependent magnetization (MB, Figure S8) curves showed clearly saturated hysteresis loops, which is characteristic of ferromagnetic materials. A minor diamagnetic signal visible at high fields in the hysteresis loops at 300 K is related to a slightly diamagnetic sample holder. Ferromagnetic behavior is in line with the results from Mössbauer spectroscopy being also consistent with the data reported in ref 50 for Ni/Fe_2O_3 nanoparticles. It is also interesting to observe that Fe_5 (the monometallic Fe/H−Y-5.1) exhibited ferromagnetic properties at both temperatures, analogously to Fe/H−Y-12 at room temperature,[12] while Fe/ZSM-12 was paramagnetic at 49.7 K.[51] Saturation magnetization both at 5 and at 300 K was the highest for Fe_5Ni_5 (Table S3) and a high saturation magnetization indicated high anisotropy.[52] In the case of the non-supported Fe−Ni samples,[28] it was observed that magnetic saturation increased linearly with increasing iron content, while in the current case of supported Fe−Ni catalysts, such a trend could not be identified. It was also reported in ref 53 that non-supported Fe−Ni alloys exhibit typically high saturation magnetization and low coercivity, and the latter indicates the presence of interparticle interactions.[28] Analogously higher saturation magnetization was observed for the Fe−Ni alloy with 15 nm particles in comparison to Ni with 33 nm particles.[54] The former one, despite of its smaller particles, exhibited higher coercivity than what was observed for Ni sample.[54] These results showed that there might be several factors affecting coercivity, not only the particle size. In the current case, at 5 K, the coercivity increased with an increasing amount of Fe and decreasing amount of Ni in the sample (Figure S9a). Coercivity for all samples also decreased with increasing temperature as was the case in Larumbe et al.[52] Worth noting that the coercivity at both 5 and 300 K temperatures increased with increasing Brønsted to Lewis acid sites ratio (Figure S9b).

Mass magnetization was also determined as a function of temperature at magnetic induction of 1 T and 50 mT (Figure S10). The results at 1 T clearly showed a rapid paramagnetic decrease in temperature-dependent magnetization (MT) curves at low temperature, above which a typical ferromagnetic behavior was observed for all samples, having Curie temperature above the highest measured temperature of 400 K. On the other hand, at 50 mT, splitting of FC and ZFC curves was observed analogously as obtained for $NiFe_2O_4$ nanoparticles in ref 55. The blocking temperatures (T_B, the maximum on the ZFC curve) for each sample at 50 mT magnetic induction increased in the following order: Fe_5Ni_5 (136 K) < Fe_8Ni_2 (255 K) < Ni_5 (257 K) < Fe_2Ni_8 (269 K) < Fe_5 (351 K). The blocking of magnetic moments originated by the anisotropy[55] and the divergency of FC and ZFC curves below the blocking temperature confirms the slow relaxation of the particles. As a comparison of the temperature dependency of magnetization between different H−Y-5.1-supported Fe-, Ni-catalysts and ferrite as well as spinel-type samples,[55] some differences were observed. In the current work, the T_B were rather high, in the

https://doi.org/10.1021/acsanm.3c00620
ACS Appl. Nano Mater. 2023, 6, 10064−10077

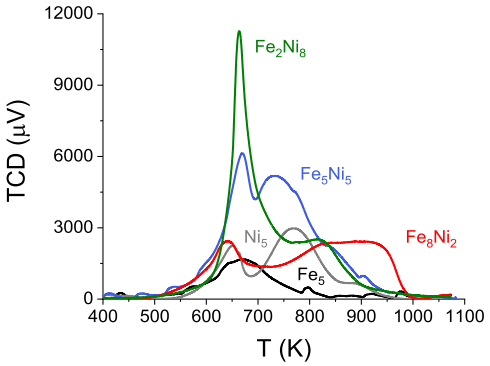

Catalyst	T_{max}	Relative peak area	
	K	*<1073 K*	*<773 K*
Fe_5	668, 798, 976	1	1
Fe_8Ni_2	638, 823-943	2.8	1.4
Fe_5Ni_5	668, 733, 903	4.2	3.5
Fe_2Ni_8	663, 818	3.7	3.2
Ni_5	650, 768, 893, 993	2.0	1.5

Figure 3. H_2-TPR profiles of Fe_5 (black), Fe_8Ni_2 (red), Fe_5Ni_5 (blue), Fe_2Ni_8 (green), and Ni_5 (grey). The relative error of TPR was less than ±3%.

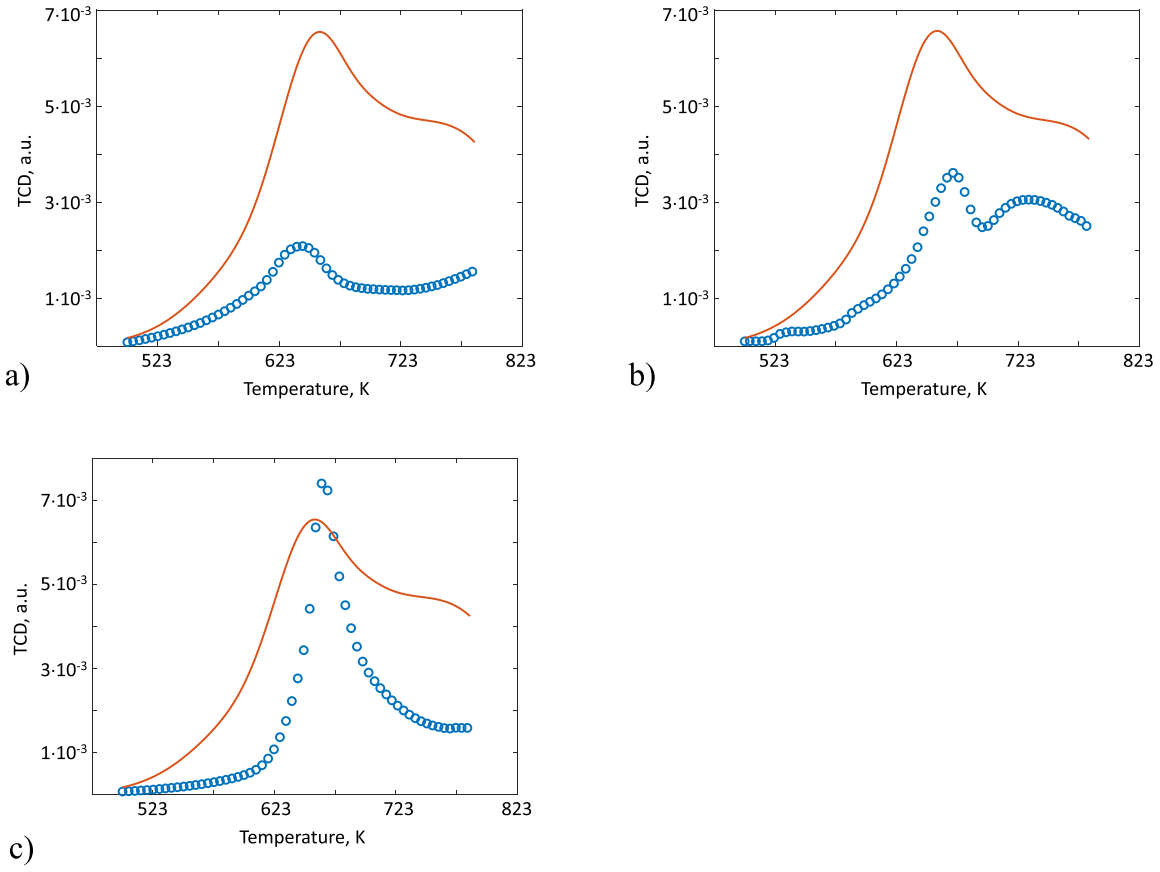

Figure 4. Model and experimental data of H_2-TPR profiles of (a) Fe_8Ni_2, (b) Fe_5Ni_5, and (c) Fe_2Ni_8.

range of 136−351 K, while in non-supported ferrites and spinel type structures, much lower T_B equal to 75 and 58 K,[55] respectively, were observed. The high T_B indicates also interparticle interactions[52] that can be achieved, e.g., via preparing the catalyst via co-precipitation. Noteworthy, in the current case, sequential incipient wetness method was used and the lowest T_B was measured for the Fe_5Ni_5 catalyst, which, however, exhibited the highest magnetic saturation. This result indicates that for supported Fe−Ni catalysts with different particle sizes and different Fe−Ni ratios, it is not fully possible to separate these effects (Figure S9c). However, the highest magnetization observed for Fe_5Ni_5 can indicate stronger interactions between Fe and Ni in the supported catalyst of this composition. The same behavior was also confirmed by the highest hydrogen consumption in TPR for this catalyst (Figure 3), and, as reported above, XRD and TEM measurements for Fe−Ni catalysts also give some indications of the interactions between Fe and Ni.

3.9. Temperature Programmed Reduction. The TPR of monometallic and bimetallic catalysts synthesized on H−Y-5.1 support (Figure 3) was performed to elucidate reducibility of these catalysts and to study the interactions between Fe and Ni nanoparticles. The TPR profile of the monometallic Fe-catalyst exhibited a broad reduction curve in the range of 548−773 K with a centered peak temperature of 668 K, which corresponds to the reduction of Fe(III) to Fe(II).[56] Additionally, two small peaks above 773 K (798, 976 K) were observed. Less than 10% of metallic Fe on H−Y zeolites in the surface layers was detected in ref 57 after reduction at 818 K with H_2. The plausible reasons for less reduction to metallic Fe^0 in the

https://doi.org/10.1021/acsanm.3c00620
ACS Appl. Nano Mater. 2023, 6, 10064−10077

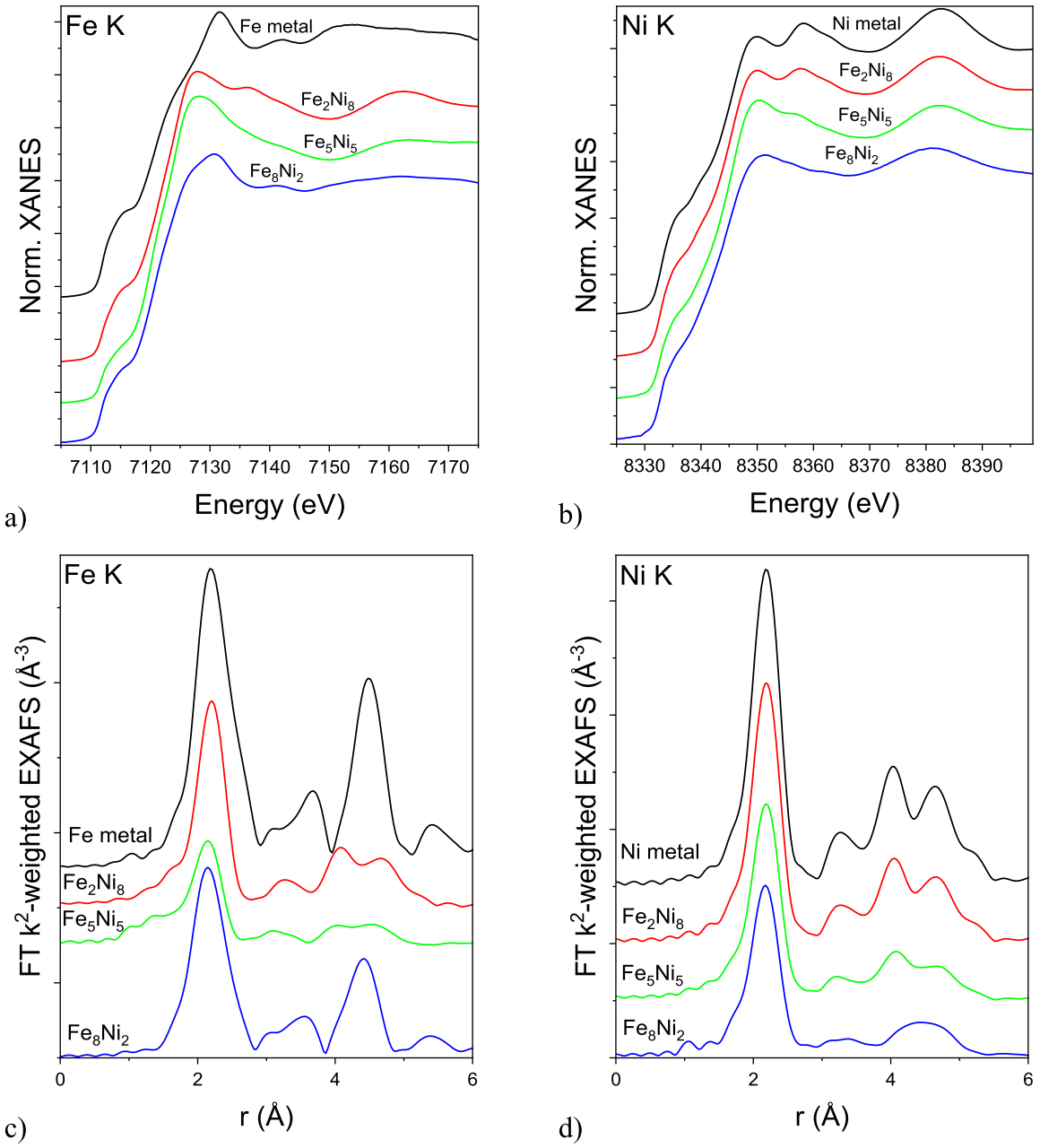

Figure 5. Normalized XANES (a,b) and FT EXAFS (c,d) spectra of reduced FeNi catalysts and the respective bulk metals (5 μm thick foils) measured at Fe K (a,c) and Ni K (b,d) edges. EXAFS spectra are not corrected for the phase shift.

Fe_5 catalyst can be attributed to the strong interactions of Fe with the structure of H−Y zeolite and catalyst synthesis and calcination conditions. The TPR profile of the monometallic Ni-catalyst exhibited a peak at 650 K that can be linked to free NiO crystallites, while peaks obtained at 768, 893, and 993 K rather reflect the reduction of other Ni-species with stronger interactions with H−Y-5.1 zeolite, as nickel aluminate or nickel silicate species.[58] It is also possible that aluminum in the sample exists outside the framework and interacts with NiO to create $NiAl_2O_4$ (nickel aluminate).[59] This is in line with the literature[59] stating that $NiAl_2O_4$ was reducible above 773 or 873 K, whereas the NiO crystallites were reduced below 773 K. However, according to the XAS data (presented below), this is unlikely for the H−Y-5.1-based catalysts used in this work.

Based on this and the peak sizes in the current work (below and above 688 K), it can be estimated that ca. 72% of Ni is bound to the H−Y-5.1 zeolite. Gac et al.[60] reported that Ni^{2+} might be reduced to Ni^{+} and finally to metallic Ni^0 in the zeolite.

Significantly different TPR patterns of the bimetallic catalysts (Figure 3), not being a superposition of TPR profiles of the monometallic catalysts, indicate interactions between iron and nickel.

This is in line with XRD, TEM, and XPS and was also supported by modeling of TPR profiles for bimetallic catalysts using the parameters obtained for the monometallic materials. Analogous results were observed for Fe, Ni, $FeNi/SiO_2$ catalyst,[24] and Ni, NiGa/MMO catalysts.[61] Formation of an intermetallic compound or an alloy may be the cause of these interactions. Furthermore, it can be assumed that Ni enhanced the reduction of Fe_2O_3 because the peaks of the bimetallic catalysts substantially increased compared to the monometallic

https://doi.org/10.1021/acsanm.3c00620
ACS Appl. Nano Mater. 2023, 6, 10064−10077

Ni and Fe catalysts. According to the literature, reduction of Fe species can be promoted by a rapid hydrogen dissociation on pre-reduced Ni sites, followed by spillover of the dissociated hydrogen to the Fe oxide sites.[24,30] The relative peak area between 373 and 1073 K (Figure 3) increased in the following order: Fe_5 (1) < Ni_5 (2) < Fe_8Ni_2 (2.8) < Fe_2Ni_8 (3.7) < Fe_5Ni_5 (4.2). The total reduction of Fe and Ni species happened at temperatures above 973 K (Figure 3). Such a high temperature can result in the sintering of the active metals and, therefore, a reasonable compromise based on the TPR results was reduction at 773 K.[58]

Modeling of TPR was performed using nonlinear regression assuming a pseudo-homogeneous reactor model with well-controlled temperature.[62−65] Detailed information about model including kinetic parameters (Table S4) and model and experimental data of H_2-TPR profiles of monometallic catalyst (Figure S11) are given into the Supporting Information.

The results presented in Figure 4 clearly indicate that the TPR profiles of bimetallic catalysts cannot be modeled using the values for monometallic counterparts confirming in a quantitative way the interactions between iron and nickel, which was especially visible for Fe_8Ni_2 and Fe_2Ni_8 catalysts.

XAS is an invaluable tool in characterization of transition metal-based catalysts. Penetration nature of X-rays allows studies directly in chemical reactors, without exposure to ambient air and the resulting reoxidation of catalysts. The method is element-specific allowing (unlike and complementary to XRD) to independently probe the electronic structure and local chemical environment (short- and medium-range ordering, up to 5 Å) around elements of interest. XAS is a bulk averaging technique providing averaged information from all atoms of a specific element in a probed volume. Here, XAS was used to investigate local structure around Fe and Ni atoms in as prepared and reduced FeNi catalysts. Noteworthy, the catalysts were reduced directly in in situ cells with a plug-flow geometry according to the protocol used for catalytic testing, then sealed in these cells under H_2 and directly measured without a need for any passivation or exposure to air.

XANES and EXAFS spectra of the calcined catalysts are depicted in Figure S12 alongside spectra of the most relevant oxidized reference compounds. Positions and shape of pre-edge and edge features in the Fe K XANES spectra (Figure S12a) correspond to Fe(III) compounds.[66] Broader features, compared to the respective bulk oxides, signify a lack of long-range ordering. Ni K XANES spectra (Figure S12b) are rather similar to NiO,[67] however, again with changed intensities and except for Fe_2Ni_8 broader features. FT Fe K EXAFS spectra (Figure S12c) contain two discernible shells, O at ca. 1.5 Å (uncorrected distance) and a second shell at ca. 2.5 Å. A lower magnitude and absence of higher shells confirm XANES findings of small nanoparticles or Fe_xO_y clusters with the smallest ones in calcined Fe_5Ni_5 catalyst. FT Ni K EXAFS spectra (Figure S12d) revealed a highly crystalline NiO structure in the calcined Fe_2Ni_8 catalyst and small NiO_x clusters in Fe_5Ni_5 (the smallest clusters) and Fe_8Ni_2 catalysts. Observed disordered Fe (III) and Ni(II) species can be Fe^{3+} and Ni^{2+} in the cationic positions of the zeolite matrix. At the same time, the Ni K XANES data does not suggest that any significant quantities of Ni aluminate spinel have been formed that would be visible via a shift of the white line peak (the most intense feature above the absorption edge) in the Ni K XANES spectra.

XAS spectra of the reduced catalysts are given in Figure 5. Edge positions in the XANES spectra confirm a reduced state of both Fe and Ni in all studied bimetallic catalysts. Bulk Fe and Ni metals crystallize in different structures under ambient conditions: bcc in the case of Fe and fcc structure for Ni. Different crystal structures result in very different XANES spectra for the respective individual metals (Figure 5a,b). The bcc structure around Ni atoms is preserved for reduced FeNi catalysts, although it is significantly distorted (and/or possibly mixed with another type of species) in the case of the Fe_8Ni_2 catalyst (Figure 5b). Electronic structure (contributing predominantly to the edge region of the XANES spectra) of Ni species in Fe_5Ni_5 and Fe_8Ni_2 catalysts is different from the bulk Ni metal and the Fe_2Ni_8 catalyst, which, for fully reduced Ni species, can only be explained via doping or alloying with Fe. Complementary Fe K XANES spectra (Figure 5a) allow for more clarity: spectra of Fe_2Ni_8 and Fe_5Ni_5 catalysts do not show any bcc Fe structure but is rather similar to the XANES spectra of fcc Ni (similar relative positions of peaks while relative intensities can be different due to electronic effects and different instrumental resolution at different absolute energies).

Different electronic and geometric structures of Fe species strongly suggest formation of fcc Fe, the only reasonable explanation for this would be fcc FeNi alloy formation. The Fe K XANES spectrum of the Fe_8Ni_2 catalyst shows a mixture of features from both bcc and fcc structures and can be modeled as a linear combination of spectra of α-Fe and fcc FeNi alloy (represented by the Fe_5Ni_5 Fe K XANES spectrum). Linear combination weights (molar fractions of the respective species) in the Fe_8Ni_2 Fe K XANES spectrum, thus, amount to 0.48(0.01) α-Fe and 0.52(0.01) fcc FeNi. Ni K EXAFS spectrum of the reduced Fe_8Ni_2 catalyst (Figure 5d) shows a broad non-resolved backscattering pattern for higher shells (3−5 Å). This could be due to averaged contributions from fcc and bcc environments that would suggest that even α-Fe nanoparticles in the Fe_8Ni_2 catalyst are doped with a certain amount of Ni.

Already qualitative analysis of the EXAFS spectra (Figure 5c,d) allows to conclude fcc structure even around Fe atoms (Figure 5c) in the reduced Fe_2Ni_8 and Fe_5Ni_5 catalysts while the scattering pattern around Fe in the reduced Fe_8Ni_2 catalyst is dominated by the bcc α-Fe structure. First shell analysis was performed on Fe K and Ni K EXAFS spectra (Figure 5c,d) to identify structural parameters such as the CN and interatomic distances (Table S5 and Figure S13). Unfortunately, due to similar scattering factors of Fe and Ni, EXAFS cannot reliably distinguish between these two types of nearest neighbors.

Fit of the Fe_2Ni_8 spectra shows identical interatomic distances around Fe and Ni atoms, which are slightly (0.005 Å) lower compared to the distances in bulk fcc Ni metal. The mean-square deviation of interatomic distances (σ^2, disorder factor) is also the same for both metals. Average first shell CNs around Fe and Ni are comparable, with Fe being slightly lower. Altogether, the observations imply nearly fcc FeNi random alloy structure, the slight difference in CNs points to somewhat Fe-enriched surface of the nanoparticles. Taking into account CN of Ni as bulk-averaged CN in the Fe_2Ni_8 nanoparticles and with an approximation of uniform spherical particles, one arrives at the mean diameter around 4−5 nm with large error bars due to uncertainty in CN determination and asymptotic behavior of the model.[68] Fe_5Ni_5 EXAFS spectra also demonstrate an fcc Ni random alloy structure with the surface slightly enriched with Fe, however with two significant

https://doi.org/10.1021/acsanm.3c00620
ACS Appl. Nano Mater. 2023, 6, 10064−10077

Table 5. Catalytic Results of Catalyst Screening after 4 h[a,b]

catalyst	conversion			yield		NL/L		cyclic products distribution			
	X_{IE}	X_{DHE}	X_{HXD}	Y_{total}	$Y_{C8-C12*}$	NL	L	DHE	PC	OFBD	OFCAD
Fe_5	100	27	3.32	0.16	0.01	84	16	100	0	0	0
Fe_8Ni_2	100	96	0.45	0.63	0.12	86	14	5	13	38**	44
Fe_5Ni_5	100	100	0.39	0.43	0.15	82	18	0	0	19	81
Fe_2Ni_8	100	100	15.48	15.8	4.5	85	15	0	10	8	82
Ni_5	100	100	0.26	0.57	0.14	80	20	0	5	7	88

[a]All data are presented in mol %. Conditions: 573 K and 3 MPa of hydrogen with 100 mL of the reaction volume, 0.1 g of catalyst, and the weight ratio of reactant-to-catalyst of 2 and 773 with respect to isoeugenol and *n*-hexadecane, respectively. [b]$Y_{C8-C12*}$—yield of jet fuel fraction without dihydroeugenol, **—oxygen-free benzene and tetralin derivatives. Notation: IE—isoeugenol, racemic mixture, DHE—dihydroeugenol, HXD—*n*-hexadecane, cat—catalyst, X—conversion, C8−C12*—jet fuels fraction without dihydroeugenol, NL—nonlinear products (branched and cyclic), L—linear products, PC—phenolic compounds, OFBD—oxygen-free benzene derivatives, and OFCAD—oxygen-free cycloalkane derivatives. The relative error of measurements was less than ±5%.

differences, compared to Fe_2Ni_8. First, the mean particle diameter is smaller with approximately 2 nm (based on CN from the Ni spectrum). Second, there are on average, two oxygen atoms per Fe (but not Ni) that signifies incomplete reduction of Fe. The difference in metal−metal CNs and presence of oxygen only in the spectrum of Fe may either be due to formation of surface-oxidized Fe-enriched FeNi alloy nanoparticles, as have been observed before,[69] or due to averaging of the EXAFS signal of unreduced Fe species, possibly cationic species in the zeolite, and reduced FeNi nanoparticles.

Spectra of the Fe_2Ni_8 do not fit to the same pattern as the other two. Coordination environment around Ni corresponds to Ni nanoparticles. Strikingly, the coordination environment around Fe atoms in the Fe_2Ni_8 spectrum corresponds to bcc (α-Fe) structure and no longer to fcc FeNi alloy. Inclusion of a certain fraction of Ni atoms in the α-Fe would explain lower interatomic distances, a higher disorder around Ni, and, especially, the broad scattering peak between 4 and 5 Å instead of well resolved shells in case of other samples (Figure 5d). Supported by XANES analysis (see above), it can be concluded that the reduced Fe_2Ni_8 sample contains two types of nanoparticles: rather small (estimated as approximately 1.2 nm) fcc Ni (doped/alloyed with Fe) and larger ca. 1.3−1.5 nm bcc Fe (according to ref 70), also doped with Ni.

According to the characterization data, interactions between iron and nickel in the catalyst were influenced by the Fe−Ni ratio, affecting reducibility, formation of the FeNi alloy and its composition, magnetic behavior, and properties such as the metal particle size and dispersion. These properties can play a crucial role in textural and structural properties significantly influencing the catalytic performance.

3.10. Catalytic Results. Catalytic properties of low-cost mono- and bimetallic bifunctional Fe−Ni/H−Y-5.1 catalysts with different metal ratios were studied in a batch reactor and are reported in detail separately.[31] In the current work, only the most pertinent catalytic data are presented (Table 5) and discussed. Co-processing of *n*-hexadecane hydroisomerization−hydrocracking with isoeugenol HDO was investigated at 573 K and 3 MPa of hydrogen with 100 mL of the reaction volume, 0.1 g of the catalyst, and the weight ratio of reactant-to-catalyst of 2 and 773 with respect to isoeugenol and *n*-hexadecane, respectively.

As described above, Fe and Ni are transition metals with similar electronic configurations forming bimetallic clusters and FeNi random alloy structures, which exhibited unique electronic and geometric properties depending on the Fe−Ni metal ratio. The catalyst with a higher content of Fe than Ni (Fe_8Ni_2) dominating with bbc α-Fe and a lower amount of FeNi alloy showed high activity in the undesired alkylation of *n*-hexadecane. On the other hand, the catalyst with equal amounts of metals (Fe_5Ni_5) exhibiting fcc FeNi random alloy structure with surface oxidized Fe-enriched FeNi alloy nanoparticles and not fully reduced bulk Ni exhibited a relatively low activity in co-processing with, however, complete selectivity toward the desired oxygen-free compounds (OFC). A lower OFC selectivity than for Fe_5Ni_5 but a significantly higher activity of co-processing than with other catalysts was obtained over the catalyst with a higher content of Ni than Fe (Fe_2Ni_8) comprising, in addition to fcc FeNi random alloy structure, also small particles of fcc Ni doped with Fe and bcc Fe doped with Ni. It is also worth noting that the monometallic Fe catalyst was almost inactive for isoeugenol HDO, and the monometallic Ni showed comparable activity as Fe_8Ni_2 and Fe_5Ni_5 but with different product distributions resulting in the highest C13−C15 selectivity.

Overall, it can be concluded that the Fe−Ni metal ratio in the catalysts has a significant impact on the formation of bimetallic clusters and FeNi alloy structures resulting in different physico-chemical properties, which led to changes in the catalytic activity and product distributions. Comparison of turnover frequency, comprising exposed moles of metals, revealed a favorable effect of the small medial metal particle size (<6 nm) on the catalytic performance in the case of *n*-hexadecane hydroisomerization−hydrocracking (Figure S14a). At the same time, the experimental data clearly showed that the bifunctionality of metal−acid catalysts is crucial in the case of isoeugenol HDO (Figure S14b). In conclusion, the optimal Fe−Ni ratio in the catalyst for either HDO of lignin-derived compounds or hydroisomerization−hydrocracking of alkanes depends on a variety of factors, including the metal interactions, metal nanoparticle size, and the metal−acid site ratio. It was also demonstrated that even a small amount of isoeugenol 0.26 wt % made *n*-hexadecane hydroisomerization−hydrocracking twofold slower.

4. CONCLUSIONS

The subsequent incipient wetness impregnation methodology was used to prepare a series of bimetallic Fe−Ni bifunctional H−Y-5.1 catalysts with different metal ratios. The catalysts along with monometallic Fe and Ni counterparts were characterized in detail by N_2 physisorption, FTIR spectroscopy using pyridine as a probe molecule, ICP−OES, XRD, TEM,

https://doi.org/10.1021/acsanm.3c00620
ACS Appl. Nano Mater. 2023, 6, 10064−10077

SEM, NMR, XPS, Mössbauer spectroscopy, magnetic measurements, TPR, and XAS.

The structure of H−Y-5.1 zeolite was retained and the specific surface area decreased by more than 40% after modification with the metals. Introduction of Fe led to a decrease of strong acid sites and an increase of mainly medium Brønsted acid sites, while introduction of Ni elevated weak and medium Lewis acid sites. The particle size of iron was ca 5 nm, while for nickel it was ca. fourfold higher. The maximum in the particle size distribution of the bimetallic Fe−Ni catalysts was decreased by the addition of Fe to monometallic Ni/H−Y-5.1. XRD revealed that the presence of Fe oxides caused a better dispersion of NiO pointing out on the interactions between iron and nickel. Existence of these interactions was also supported by a high blocking temperature obtained from magnetic measurements, TEM, modeling of TPR profiles, and XPS. Moreover, according to XPS, more iron was on the catalyst surface compared to nickel. Comparison of results from XPS and Mössbauer spectroscopy showed that initially present Fe^{3+} originating from the iron(III) nitrate precursor was fully reduced at 773 K only on the surface, but not in the bulk of the catalyst. Both Mössbauer spectroscopy and magnetic measurements confirmed ferromagnetic behavior of all prepared catalysts. Quasi in situ XAS confirmed a close contact between Fe and Ni nanoparticles in the reduced catalysts with formation of surface Fe-enriched fcc FeNi random alloys in Fe_2Ni_8 and Fe_5Ni_5 catalysts as well as a mixture of Ni-doped bcc α-Fe and fcc FeNi nanoparticles in Fe_8Ni_2. XAS has also confirmed the trend of decreasing average nanoparticle size with increasing Fe content.

The synergistic effect of Fe and Ni metals was investigated in the co-processing of fossil feedstock with lignin-derived model compound, isoeugenol. Catalytic results showed that both the reaction rate and product distribution strongly depend on the Fe−Ni metal ratio, the metal interactions, the FeNi alloy structure, the metal nanoparticle size, and the metal−acid site ratio in the catalysts.

■ ASSOCIATED CONTENT

Supporting Information

The Supporting Information is available free of charge at https://pubs.acs.org/doi/10.1021/acsanm.3c00620.

> Textural properties, XRD patterns, TEM images and metal particle size distribution, SEM images, NMR spectra, XPS spectra, Mössbauer parameters and spectra, magnetic measurements, modeling of TPR profiles, model data of H_2-TPR profiles, XANES and EXAFS data, and catalytic data (PDF)

■ AUTHOR INFORMATION

Corresponding Author

Dmitry Yu. Murzin − *Johan Gadolin Process Chemistry Centre, Åbo Akademi University, Turku/Åbo 20500, Finland;* orcid.org/0000-0003-0788-2643; Email: dmurzin@abo.fi

Authors

Zuzana Vajglová − *Johan Gadolin Process Chemistry Centre, Åbo Akademi University, Turku/Åbo 20500, Finland*

Bibesh Gauli − *Johan Gadolin Process Chemistry Centre, Åbo Akademi University, Turku/Åbo 20500, Finland*

Päivi Mäki-Arvela − *Johan Gadolin Process Chemistry Centre, Åbo Akademi University, Turku/Åbo 20500, Finland;* orcid.org/0000-0002-7055-9358

Narendra Kumar − *Johan Gadolin Process Chemistry Centre, Åbo Akademi University, Turku/Åbo 20500, Finland*

Kari Eränen − *Johan Gadolin Process Chemistry Centre, Åbo Akademi University, Turku/Åbo 20500, Finland*

Johan Wärnå − *Johan Gadolin Process Chemistry Centre, Åbo Akademi University, Turku/Åbo 20500, Finland*

Robert Lassfolk − *Johan Gadolin Process Chemistry Centre, Åbo Akademi University, Turku/Åbo 20500, Finland;* orcid.org/0000-0002-6555-3488

Irina L. Simakova − *Boreskov Institute of Catalysis, Novosibirsk 630090, Russia;* orcid.org/0000-0002-5138-4847

Igor P. Prosvirin − *Boreskov Institute of Catalysis, Novosibirsk 630090, Russia;* orcid.org/0000-0002-0351-5128

Markus Peurla − *Institute of Biomedicine, University of Turku, Turku 20520, Finland*

Johan Kaarle Mikael Lindén − *Faculty of Science and Engineering/Physics, Åbo Akademi University, Turku/Åbo 20520, Finland;* orcid.org/0000-0002-6155-3026

Hannu Huhtinen − *Wihuri Physical Laboratory, Department of Physics and Astronomy, University of Turku, Turku 20014, Finland*

Petriina Paturi − *Wihuri Physical Laboratory, Department of Physics and Astronomy, University of Turku, Turku 20014, Finland*

Dmitry E. Doronkin − *Institute of Chemical Technology and Polymer Chemistry, and Institute of Catalysis Research and Technology, Karlsruhe Institute of Technology, Karlsruhe 76131, Germany;* orcid.org/0000-0003-3930-3204

Complete contact information is available at: https://pubs.acs.org/10.1021/acsanm.3c00620

Notes

The authors declare no competing financial interest.

■ ACKNOWLEDGMENTS

The authors are grateful to Business Finland for funding through the project: Catalytic Slurry Hydrotreatment. Electron microscopy samples were processed and analyzed at the Electron Microscopy Laboratory, Institute of Biomedicine, University of Turku, which receives financial support from Biocenter Finland. I.S. is grateful for the support from the Ministry of Science and Higher Education of the Russian Federation, under the governmental order for Boreskov Institute of Catalysis (project no. AAAAA21-121011390055-8). DESY (Hamburg, Germany), a member of the Helmholtz Association HGF, is acknowledged for the provision of experimental facilities. Parts of this research were carried out at the light source PETRA III at DESY, a member of the Helmholtz Association (HGF). The authors would like to thank Dr. Edmund Welter for his assistance in using the beamline P65.

■ REFERENCES

(1) Robinson, A. M.; Hensley, J. E.; Medlin, J. W. Bifunctional Catalysts for Upgrading of Biomass-Derived Oxygenates: A Review. *ACS Catal.* **2016**, *6*, 5026−5043.

(2) Mäki-Arvela, P.; Murzin, D. Y. Hydrodeoxygenation of Lignin-Derived Phenols: From Fundamental Studies towards Industrial Applications. *Catalysts* **2017**, *7*, 265.
(3) European Commission. Directive (EU) 2018/2001 of the European Parliament and of the Council of 11 December 2018 on the promotion of the use of energy from renewable sources (recast). *Off. J. Eur. Union* **2018**, *L328*, 82−209.
(4) Hachemi, I.; Jenistova, K.; Mäki-Arvela, P.; Kumar, N.; Eränen, K.; Hemming, J.; Murzin, D. Y. Comparative Study of Sulfur-Free Nickel and Palladium Catalysts in Hydrodeoxygenation of Different Fatty Acid Feedstocks for Production of Biofuels. *Catal. Sci. Technol.* **2016**, *6*, 1476−1487.
(5) Sagi, D.; Baladincz, P.; Varga, Z.; Hancsok, J. Co-processing of FCC Light Cycle Oil and Waste Animal Fats with Straight Run Gas Oil Fraction. *J. Cleaner Prod.* **2016**, *111*, 34−41.
(6) Pujro, R.; Panero, M.; Bertero, M.; Sedran, U.; Falco, M. Hydrogen Transfer between Hydrocarbons and Oxygenated Compounds in Coprocessing Bio-Oils in Fluid Catalytic Cracking. *Energy Fuels* **2019**, *33*, 6473−6482.
(7) Bezergianni, S.; Dimitriadis, A.; Karonis, D. Diesel decarbonization via effective catalytic Co-hydroprocessing of residual lipids with gas-oil. *Fuel* **2014**, *136*, 366−373.
(8) Kumar, A.; Sharma, S. Potential Non-Edible Oil Resources as Biodiesel Feedstock: An Indian Perspective. *Renewable Sustainable Energy Rev.* **2011**, *15*, 1791−1800.
(9) Azkaar, M.; Vajglová, Z.; Mäki-Arvela, P.; Aho, A.; Kumar, N.; Palonen, H.; Eränen, K.; Peurla, M.; Kulikov, L.; Maximov, A.; Mondelli, C.; Pérez-Ramírez, J.; Murzin, D. Y. Hydrocracking of Hexadecane to Jet Fuel Components over Hierarchical Ru-Modified Faujasite Zeolite. *Fuel* **2020**, *278*, 118193.
(10) Kaka khel, T.; Mäki-Arvela, P.; Azkaar, M.; Vajglová, Z.; Aho, A.; Hemming, J.; Peurla, M.; Eränen, K.; Kumar, N.; Murzin, D. Y. Hexadecane Hydrocracking for Production of Jet Fuels from Renewable Diesel over Proton and Metal Modified H-Beta Zeolites. *Mol. Catal.* **2019**, *476*, 110515.
(11) Al-Muttaqii, M.; Kurniawansyah, F.; Prajitno, D. H.; Roesyadi, A. Hydrocracking of Coconut Oil over Ni-Fe/HZSM-5 Catalyst to Produce Hydrocarbon Biofuel. *Indones. J. Chem.* **2019**, *19*, 319−327.
(12) Aho, A.; Kumar, N.; Lashkul, A. V.; Eränen, K.; Ziolek, M.; Decyk, P.; Salmi, T.; Holmbom, B.; Hupa, M.; Murzin, D. Yu. Catalytic Upgrading of Woody Biomass Derived Pyrolysis Vapours over Iron Modified Zeolites in a Dual-Fluidized Bed Reactor. *Fuel* **2010**, *89*, 1992−2000.
(13) Lindfors, C.; Mäki-Arvela, P.; Paturi, P.; Aho, A.; Eränen, K.; Hemming, J.; Peurla, M.; Kubička, D.; Simakova, I. L.; Murzin, D. Y. Hydrodeoxygenation of Isoeugenol over Ni- and Co-Supported Catalysts. *ACS Sustainable Chem. Eng.* **2019**, *7*, 14545−14560.
(14) Olcese, R. N.; Bettahar, M.; Petitjean, D.; Malaman, B.; Giovanella, F.; Dufour, A. Gas-Phase Hydrodeoxygenation of Guaiacol over Fe/SiO_2 Catalyst. *Appl. Catal., B* **2012**, *115*−*116*, 63−73.
(15) Olcese, R. N.; Francois, J.; Bettahar, M. M.; Petitjean, D.; Dufour, A. Hydrodeoxygenation of Guaiacol, A Surrogate of Lignin Pyrolysis Vapors, Over Iron Based Catalysts: Kinetics and Modeling of the Lignin to Aromatics Integrated Process. *Energy Fuels* **2013**, *27*, 975−984.
(16) Peters, J. E.; Carpenter, J. R.; Dayton, D. C. Anisole and Guaiacol Hydrodeoxygenation Reaction Pathways over Selected Catalysts. *Energy Fuels* **2015**, *29*, 909−916.
(17) Rezaei, P. S.; Shafaghat, H.; Daud, W. Aromatic Hydrocarbon Production by Catalytic Pyrolysis of Palm Kernel Shell Waste using a Bifunctional Fe/HBeta Catalyst: Effect of Lignin-Derived Phenolics on Zeolite Deactivation. *Green Chem.* **2016**, *18*, 1684−1693.
(18) Sirous-Rezaei, P.; Jae, J.; Ha, J. M.; Ko, C. H.; Kim, J. M.; Jeon, J. K.; Park, Y. K. Mild Hydrodeoxygenation of Phenolic Lignin Model Compounds over a FeReOx/ZrO_2 Catalyst: Zirconia and Rhenium Oxide as Efficient Dehydration Promoters. *Green Chem.* **2018**, *20*, 1472−1483.
(19) Nie, L.; De Souza, P. M.; Noronha, F. B.; An, W.; Sooknoi, T.; Resasco, D. E. Selective Conversion of m-Cresol to Toluene over Bimetallic Ni-Fe Catalysts. *J. Mol. Catal. A: Chem.* **2014**, *388*−*389*, 47−55.
(20) Xu, X. W.; Jiang, E. C.; Li, Z. Y.; Sun, Y. BTX from Anisole by Hydrodeoxygenation and Transalkylation at Ambient Pressure with Zeolite Catalysts. *Fuel* **2018**, *221*, 440−446.
(21) Tieuli, S.; Mäki-Arvela, P.; Peurla, M.; Eränen, K.; Warna, J.; Cruciani, G.; Menegazzo, F.; Murzin, D. Yu.; Signoretto, M. Hydrodeoxygenation of Isoeugenol over Ni-SBA-15: Kinetics and Modelling. *Appl. Catal., A* **2019**, *580*, 1−10.
(22) Fang, H. H.; Zheng, J. W.; Luo, X. L.; Du, J. M.; Roldan, A.; Leoni, S.; Yuan, Y. Z. Product Tunable Behavior of Carbon Nanotubes-Supported Ni-Fe Catalysts for Guaiacol Hydrodeoxygenation. *Appl. Catal., A* **2017**, *529*, 20−31.
(23) Han, Q.; Rehman, M. U.; Wang, J. H.; Rykov, A.; Gutierrez, O. Y.; Zhao, Y. J.; Wang, S. P.; Ma, X. B.; Lercher, J. A. The Synergistic Effect between Ni Sites and Ni-Fe Alloy Sites on Hydrodeoxygenation of Lignin-Derived Phenols. *Appl. Catal., B* **2019**, *253*, 348−358.
(24) Han, D.; Yin, W.; Luo, D.; He, H.; Wang, S.; Xia, S. Hydrodeoxygenation of Aliphatic Acid over NiFe Intermetallic Compounds: Insights into the Mechanism via Model Compound Study. *Fuel* **2021**, *305*, 121545.
(25) Shafaghat, H.; Rezaei, P. S.; Daud, W. Catalytic Hydrodeoxygenation of Simulated Phenolic Bio-Oil to Cycloalkanes and Aromatic Hydrocarbons over Bifunctional Metal/Acid Catalysts of Ni/HBeta, Fe/HBeta and NiFe/HBeta. *J. Ind. Eng. Chem.* **2016**, *35*, 268−276.
(26) Boron, P.; Chmielarz, L.; Gurgul, J.; Latka, K.; Gil, B.; Marszalek, B.; Dzwigaj, S. Influence of Iron State and Acidity of Zeolites on the Catalytic Activity of FeHBEA, FeHZSM-5 and FeHMOR in SCR of NO with NH_3 and N_2O Decomposition. *Microporous Mesoporous Mater.* **2015**, *203*, 73−85.
(27) Mibu, K.; Kojima, T.; Mizuguchi, M.; Takanashi, K. Local Structure and Magnetism of L1(0)-Type FeNi Alloy Films with Perpendicular Magnetic Anisotropy Studied through Fe-57 Nuclear Probes. *J. Phys. D: Appl. Phys.* **2015**, *48*, 205002.
(28) Dijith, K. S.; Aiswarya, R.; Praveen, M.; Pillai, S.; Surendran, K. P. Polyol Derived Ni and NiFe Alloys for Effective Shielding of Electromagnetic Interference. *Mater. Chem. Front.* **2018**, *2*, 1829−1841.
(29) Li, J.; Tang, W. J.; Huang, J. W.; Jin, J.; Ma, J. T. Polyethyleneimine Decorated Graphene Oxide-Supported Ni1-xFex Bimetallic Nanoparticles as Efficient and Robust Electrocatalysts for Hydrazine Fuel Cells. *Catal. Sci. Technol.* **2013**, *3*, 3155−3162.
(30) Yu, X. B.; Chen, J. X.; Ren, T. Y. Promotional Effect of Fe on Performance of Ni/SiO_2 for Deoxygenation of Methyl Laurate as a Model Compound to Hydrocarbons. *RSC Adv.* **2014**, *4*, 46427−46436.
(31) Vajglová, Z.; Gauli, B.; Mäki-Arvela, P.; Simakova, I. L.; Kumar, N.; Eränen, K.; Tirri, T.; Lassfolk, R.; Peurla, M.; Doronkin, D.; Murzin, D. Y. Co-Processing of Fossil Feedstock with Lignin-Derived Model Compound Isoeugenol over Fe-Ni/H-Y-5.1 Catalysts. *J. Catal.* **2023**, *421*, 101−116.
(32) Emeis, C. A. Determination of Integrated Molar Extinction Coefficients for Infrared Absorption Bands of Pyridine Adsorbed on Solid Acid Catalysts. *J. Catal.* **1993**, *141*, 347−354.
(33) Moulder, J. F.; Stickle, W. F.; Sobol, P. E.; Bomben, K. D. *Handbook of X-Ray Photoelectron Spectroscopy*; PerkinElmer Corporation: United State of America, 1992.
(34) Scofield, J. H. Hartree-Slater Subshell Photoionization Cross-Sections at 1254 and 1487EV. *J. Electron Spectrosc. Relat. Phenom.* **1976**, *8*, 129−137.
(35) Ravel, B.; Newville, M. ATHENA, ARTEMIS, HEPHAESTUS: Data Analysis for X-ray Absorption Spectroscopy using IFEFFIT. *J. Synchrotron Radiat.* **2005**, *12*, 537−541.
(36) Vajglová, Z.; Kumar, N.; Mäki-Arvela, P.; Eränen, K.; Peurla, M.; Hupa, L.; Nurmi, M.; Toivakka, M.; Murzin, D. Yu. Synthesis and Physicochemical Characterization of Shaped Catalysts of Beta and Y

https://doi.org/10.1021/acsanm.3c00620
ACS Appl. Nano Mater. 2023, 6, 10064−10077

Zeolites for Cyclization of Citronellal. *Ind. Eng. Chem. Res.* **2019**, *58*, 18084−18096.
(37) Lorenzelli, V.; Busca, G. Infrared Studies of the Surface of α-Fe_2O_3. *Mater. Chem. Phys.* **1985**, *13*, 261−281.
(38) Kubička, D.; Kumar, N.; Venalainen, T.; Karhu, H.; Kubičková, I.; Osterholm, H.; Murzin, D. Yu. Metal-Support Interactions in Zeolite-Supported Noble Metals: Influence of Metal Crystallites on the Support Acidity. *J. Phys. Chem. B* **2006**, *110*, 4937−4946.
(39) Li, C.; Xu, G. Y.; Zhai, Y. X.; Liu, X. H.; Ma, Y. F.; Zhang, Y. Hydrogenation of Biomass-Derived Ethyl Levulinate into Gamma-Valerolactone by Activated Carbon Supported Bimetallic Ni and Fe Catalysts. *Fuel* **2017**, *203*, 23−31.
(40) Yang, X. Y.; Cheng, X. W.; Elzatahry, A. A.; Chen, J. Y.; Alghamdi, A.; Deng, Y. H. Recyclable Fenton-Like Catalyst Based on Zeolite Y Supported Ultrafine, Highly-Dispersed Fe_2O_3 Nanoparticles for Removal of Organics under Mild Conditions. *Chin. Chem. Lett.* **2019**, *30*, 324−330.
(41) Zhang, S. P.; Zhang, H. L.; Liu, X. Z.; Zhu, S. G.; Hu, L. L.; Zhang, Q. Upgrading of Bio-Oil from Catalytic Pyrolysis of Pretreated Rice Husk over Fe-Modified ZSM-5 Zeolite Catalyst. *Fuel Process. Technol.* **2018**, *175*, 17−25.
(42) Li, Z. Y.; Yi, W. M.; Li, Z. H.; Bai, X. Y.; Fu, P.; Tian, C. Y.; Zhang, Y. C. Hydrodeoxygenation of Bio-Oil and Model Compounds for Production of Chemical Materials at Atmospheric Pressure over Nickel-Based Zeolite Catalysts. *Energy Sources, Part A* **2020**, 1−13.
(43) Štekrová, M.; Mäki-Arvela, P.; Kumar, N.; Behravesh, E.; Aho, A.; Balme, Q.; Volcho, K. P.; Salakhutdinov, N. F.; Murzin, D. Yu. Prins Cyclization: Synthesis of Compounds with Tetrahydropyran Moiety over Heterogeneous Catalysts. *J. Mol. Catal. A: Chem.* **2015**, *410*, 260−270.
(44) Perezpariente, J.; Sanz, J.; Fornes, V.; Corma, A. 29Si and 27Al MAS NMR study of zeolite $beta; with different Si/Al Ratios. *J. Catal.* **1990**, *124*, 217−223.
(45) Kolodziejski, W.; Zicovichwilson, C.; Corell, C.; Perez-Pariente, J.; Corma, A. 27Al and 29Si MAS NMR Study of Zeolite MCM-22. *J. Phys. Chem.* **1995**, *99*, 7002−7008.
(46) Van Bokhoven, J. A.; Koningsberger, D. C.; Kunkeler, P.; Van Bekkum, H.; Kentgens, A. P. M. Stepwise Dealumination of Zeolite Beta at Specific T-Sites Observed with ^{27}Al MAS and ^{27}Al MQ MAS NMR. *J. Am. Chem. Soc.* **2000**, *122*, 12842−12847.
(47) Nagai, Y.; Senda, M.; Toshima, T. XPS Investigations of Ni-Fe Alloy and Fe Films. *Jpn. J. Appl. Phys.* **1987**, *26*, 1131−1134.
(48) Foster, S. L.; Acharya, P.; Abolhassani, M.; Watson, S.; Shinn, S.; Greenlee, L. F. Nickel-Iron Alloy Nanoparticle Characteristics Pre- and Post-Reaction With Orange G. *IEEE Open Journal of Nanotechnology*; Institute of Electrical and Electronics Engineers, 2021; Vol. 2, pp 16−25.
(49) Yasar, E.; Erdem, U.; Akif Tuna, M.; Armagan, O.; Kirindi, T. The Effect of Ti Content on Alpha Martensite Phase Transformation, and Magnetic Properties by Mössbauer Spectroscopy in Fe-30%Ni-x% Ti (wt%) Alloys. *Acta Phys. Pol., A* **2018**, *133*, 1165−1169.
(50) Nakhjavan, B.; Tahir, M. N.; Natalio, F.; Panthofer, M.; Gao, H.; Dietzsch, M.; Andre, R.; Gasi, T.; Ksenofontov, V.; Branscheid, R.; Kolb, U.; Tremel, W. Ni@Fe_2O_3 Heterodimers: Controlled Synthesis and Magnetically Recyclable Catalytic Application for Dehalogenation Reactions. *Nanoscale* **2012**, *4*, 4571−4577.
(51) Kumar, N.; Mäki-Arvela, P.; Diaz, S. F.; Aho, A.; Demidova, Y.; Linden, J.; Shepidchenko, A.; Tenhu, M.; Salonen, J.; Laukkanen, P.; Lashkul, A.; Dahl, J.; Sinev, I.; Leino, A. R.; Kordas, K.; Salmi, T.; Murzin, D. Y. Isomerization of Alpha-Pinene Oxide Over Iron-Modified Zeolites. *Top. Catal.* **2013**, *56*, 696−713.
(52) Larumbe, S.; Gomez-Polo, C.; Perez-Landazabal, J. I.; Garcia-Prieto, A.; Alonso, J.; Fdez-Gubieda, M. L.; Cordero, D.; Gomez, J. Ni Doped Fe_3O_4 Magnetic Nanoparticles. *J. Nanosci. Nanotechnol.* **2012**, *12*, 2652−2660.
(53) Pfeifer, F.; Radeloff, C. Soft Magnetic Ni-Fe and Co-Fe Alloys - Some Physical and Metallurgical Aspects. *J. Magn. Magn. Mater.* **1980**, *19*, 190−207.
(54) Ali, B.; Tasirin, S. M.; Aminayi, P.; Yaakob, Z.; Ali, N. T.; Noori, W. Non-Supported Nickel-Based Coral Sponge-Like Porous Magnetic Alloys for Catalytic Production of Syngas and Carbon Bio-Nanofilaments via a Biogas Decomposition Approach. *Nanomater* **2018**, *8*, 1053.
(55) Iraqui, S.; Kashyap, S. S.; Rashid, M. H. $NiFe_2O_4$ Nanoparticles: an Efficient and Reusable Catalyst for the Selective Oxidation of Benzyl Alcohol to Benzaldehyde under Mild Conditions. *Nanoscale Adv.* **2020**, *2*, 5790−5802.
(56) Nagai, M.; Uchino, O.; Okubo, J.; Omi, S. TPR and XPS studies of Iron-Exchanged Y Zeolites and their Activity during Dibenzothiophene Hydrodesulfurization. *Stud. Surf. Sci. Catal.* **1997**, *105*, 989−995.
(57) Novakova, J.; Kubelkova, L.; Wichterlova, B.; Juska, T.; Dolejsek, Z. Properties of Different Fe(III) Species Introduced into NH_4-Y Zeolites. *Zeolites* **1982**, *2*, 17−22.
(58) Czuma, N.; Zarebska, K.; Motak, M.; Galvez, M. E.; Da Costa, P. Ni/Zeolite X Derived from Fly Ash as Catalysts for CO_2 Methanation. *Fuel* **2020**, *267*, 117139.
(59) Misi, S. E. E.; Ramli, A.; Rahman, F. H. Characterization of the Structure Feature of Bimetallic Fe-Ni Catalysts. *J. Appl. Sci.* **2011**, *11*, 1297−1302.
(60) Gac, W.; Greluk, M.; Slowik, G.; Millot, Y.; Valentin, L.; Dzwigaj, S. Effects of Dealumination on the Performance of Ni-Containing BEA Catalysts in Bioethanol Steam Reforming. *Appl. Catal., B* **2018**, *237*, 94−109.
(61) Zhao, N.; Zheng, Y.; Chen, J. Remarkably Reducing Carbon Loss and H_2 Consumption on Ni−Ga Intermetallic Compounds in Deoxygenation of Methyl Esters to Hydrocarbons. *J. Energy Chem.* **2020**, *41*, 194−208.
(62) Moulijn, J. A.; Van Leeuwen, P. W. N. M.; Van Santen, R. A. *Catalysis: An Integrated Approach to Homogeneous, Heterogeneous and Industrial Catalysis*; Elsevier Science Publishers B. V.: Amsterdam, 1993.
(63) Kanervo, J. M.; Krause, A. O. I. Kinetic Analysis of Temperature-Programmed Reduction: Behavior of a CrO_x/Al_2O_3 Catalyst. *J. Phys. Chem. B* **2001**, *105*, 9778−9784.
(64) Haario, H. *Modest Users's Guide 6.0*; Profmath Oy: Helsinki, 2001.
(65) Murzin, D. Y.; Salmi, T. *Catalytic Kinetics*; Elsevier B.V.: Amsterdam, 2016.
(66) Boubnov, A.; Lichtenberg, H.; Mangold, S.; Grunwaldt, J.-D. Identification of the iron oxidation state and coordination geometry in iron oxide- and zeolite-based catalysts using pre-edge XAS analysis. *J. Synchrotron Radiat.* **2015**, *22*, 410−426.
(67) Hengst, K.; Ligthart, D. A. J. M.; Doronkin, D.; Walter, K.; Kleist, W.; Hensen, E.; Grunwaldt, J.-D. Continuous Synthesis of γ−Valerolactone in a Trickle-bed Reactor over Supported Nickel Catalysts. *Ind. Eng. Chem. Res.* **2017**, *56*, 2680−2689.
(68) Puig-Molina, A.; Cano, F. M.; Janssens, T. V. W. The Cu Promoter in an Iron−Chromium-Oxide Based Water−Gas Shift Catalyst under Industrial Conditions Studied by in-Situ XAFS. *J. Phys. Chem. C* **2010**, *114*, 15410−15416.
(69) Serrer, M.-A.; Gaur, A.; Jelic, J.; Weber, S.; Fritsch, C.; Clark, A. H.; Saraci, E.; Studt, F.; Grunwaldt, J.-D. Structural Dynamics in Ni−Fe Catalysts during CO_2 Methanation − Role of Iron Oxide Clusters. *Catal. Sci. Technol.* **2020**, *10*, 7542−7554.
(70) Borowski, M. Size Determination of Small Cu-Clusters by EXAFS. *J. Phys., IV France* **1997**, *7*, C2-259−C2-260.

https://doi.org/10.1021/acsanm.3c00620
ACS Appl. Nano Mater. 2023, 6, 10064−10077